Argonne NATIONAL LABORATORY

ANL-AMMT-005

In-situ and ex-situ characterization of ion-irradiated AM materials

Nuclear Science and Engineering Division

ANL-AMMT-005

In-situ and *ex-situ* characterization of ion-irradiated AM materials

prepared by
Wei-Ying Chen, Yiren Chen, Peter Baldo
Nuclear Science and Engineering Division, Argonne National Laboratory

Josh Hlavenka, Dzmitry Harbaruk
Experimental Operations and Facilities Division, Argonne National Laboratory

July 2023

ABSTRACT

Additive manufacturing (AM) has attracted increasing attention in recent years as a new way of making high-quality components for nuclear reactors. While AM materials are compositionally similar to their conventionally produced counterparts, they do possess different microstructures, such as dislocation cells and chemical inhomogeneity, that can lead to different mechanical properties and performance behavior. In this study, the irradiation response of AM materials was investigated. *In-situ* and *ex-situ* ion irradiations were performed on laser powder bed fusion (LPBF) 316L and 316H stainless steels (SS) at 300 and 600°C. The influence of the dislocation cell structure on the evolution of irradiation-induced dislocation loops was evident at 600ºC, but was much weaker at 300ºC. No voids were observed with the *in-situ* ion irradiation up to 10 dpa at both temperatures. Post-irradiation energy dispersive spectroscopy showed radiation-induced segregation (RIS) near grain boundaries and the formation of Cr-rich oxides throughout the matrix. The extent of segregation at dislocation cell walls varies with dose. Nanoindentation tests performed on the LPBF316L SS irradiated at 600ºC showed a complex dose dependence with softening at low doses and hardening at high doses.

TABLE OF CONTENTS

Abstract ii
List of Figures iv
List of Tables vi
1 Introduction 1
2 Experimental 2
2.1 Materials and specimen preparations 2
2.2 *In-situ* and ex-situ ion irradiations 3
2.3 Post-irradiation examination 5
3 Results and Discussion 6
3.1 TEM examinations of as-printed microstructures 6
3.2 Defect evolution under *in-situ* ion irradiation 9
3.2.1 Defect evolution in LPBF 316H SS 9
3.2.2 Defect evolution in LPBF 316L SS 10
3.2.3 RIS in LPBF316H SS 15
3.3 Nanoindentation tests on ex-situ irradiated specimens 18
4 Summary 20
Acknowledgment 21
References: 22

LIST OF FIGURES

Figure 1. The IVEM-Tandem Facility at Argonne National Laboratory 4
Figure 2. Specimen chamber and the beam lines for ex-situ ion irradiation. 4
Figure 3. TEM results of as-printed LPBF316L-1: (a) low-magnification BF TEM image. (b) high-magnification BF TEM image. (c) diffraction pattern taken at a two-beam condition of g = 200 near 001 zone axis. (d)(e) under-focused TEM images with a defocus of 5 μm. The red arrows indicate the oxide particles. (f) the size distribution of the oxide particles. (g) TEM image of an inclusion. (h) EDS spectrum of the inclusion. 7
Figure 4. TEM images of as-printed LPBF316L-2: (a) low-magnification BF TEM image. The inset is the diffraction pattern taken at 011 zone axis. (b) BF TEM image of a dislocation cell. (c) the corresponding DF TEM image of the dislocation cell. The imaging condition for (b) and (c) is a two-beam condition with g = 200 near 011 zone axis. 8
Figure 5. TEM images of as-printed LPBF316H SS: (a) Low-magnification BF TEM image. (b) and (c) Higher-magnification BF and DF TEM images of a dislocation cell. The inset is the corresponding diffraction condition for the images (g = 200 near 011 zone axis). 8
Figure 6. EDS composition maps of as-printed LPBF316H. Magnification is 20K. 9
Figure 7. A set of same area BF TEM images of LPBF316H *in-situ* irradiated with 1 MeV Kr ions at 600ºC to (a) 0.3 dpa, (b) 0.6 dpa, (c) 1 dpa, (d) 3 dpa and (e) 5 dpa. (e) the corresponding diffraction pattern of the two-beam condition (g = 200 near 011 zone axis) used for the set. .. 11
Figure 8. A set of same area BF TEM images of LPBF316H *in-situ* irradiated with 1 MeV Kr ions at 300ºC to (a) 0.3 dpa, (b) 0.6 dpa, (c) 1 dpa, (d) 3 dpa and (e) 5 dpa. The inset is the diffraction pattern indicating the two-beam condition of g = 200 near 011 zone axis. (f) a high-magnification image of the 1-dpa sample. The red arrows indicate the edge-on faulted dislocation loops. 12
Figure 9. BF TEM image of LPBF316L-1 *in-situ* irradiated with 1 MeV Kr ions at 600ºC to 1 dpa. The inset is the imaging condition -- a two-beam condition with g = **111** near 011 zone axis. 13
Figure 10. BF TEM image of LPBF316L-2 *in-situ* irradiated with 1 MeV Kr ions at 600ºC to 1 dpa. The inset diffraction pattern is the imaging condition -- a two-beam condition with g = 200 near 011 zone axis. 14
Figure 11. BF TEM image of LPBF316L-1 *in-situ* irradiated with 1 MeV Kr ions at 300ºC to 1 dpa. The inset diffraction pattern is the imaging condition -- a two-beam condition with g = 200 near 001 zone axis. 14
Figure 12. BF TEM image of LPBF316L-2 *in-situ* irradiated with 1 MeV Kr ions at 300ºC to 1 dpa. The inset diffraction pattern shows the imaging condition -- a two-beam condition with g = 200 near 011 zone axis. 15
Figure 13. EDS maps of LPBF316H *in-situ* irradiated at 600ºC with 1 MeV Kr ions to 5 dpa. The red dashed curves highlight the boundary of a denuded zone of chromium oxides in the vicinity of the grain boundary. All the EDS maps were characteristic x-ray intensity maps, except for iron, which is a compositional map. The magnification is 20K. 16
Figure 14. EDS maps of LPBF316H annealed at 600ºC inside a TEM for 90 minutes. All maps are intensity maps. The magnification is 20K. 17

Figure 15. EDS maps of LPBF316H *in-situ* irradiated at 600ºC with 1 MeV Kr ions to 5 dpa. All elemental maps are the characteristic x-ray intensity maps. The magnification is 20K..... 18
Figure 16. Load-controlled nanoindentation measurements on LPBF316L-1 irradiated with 4 MeV Ni ions at 600ºC..... 19

LIST OF TABLES

Table 1. Compositions (wt.%) of the LPBF316L and LPBF316H stainless steels 2
Table 2. Irradiation parameters of *in-situ* ion irradiation..... 4
Table 3. Irradiation parameters of ex-situ ion irradiation..... 5

1 Introduction

The development of metal additive manufacturing (AM) has provided new opportunities for advancing material technologies. Complex geometries can be fabricated rapidly and cost effectively with AM, leading to a wide range of innovations in the field of material and manufacturing. As such, AM materials have attracted increasing attention in recent years as a new way to make high-quality components with added flexibilities in design and customization. While AM and conventionally produced materials are compositionally similar, they do possess different microstructures. Porosity, anisotropic grains, inclusions, dislocation cell structure, and chemical inhomogeneity resulting from printing process are often observed in AM materials. These microstructures and their behavior under service conditions must be evaluated carefully before AM materials can be widely adopted. With the objective of accelerating the development of advanced materials and manufacturing technologies, the service performance of AM materials for nuclear applications is of interest to the Advanced Materials and Manufacturing Technologies (AMMT) program under the Department of Energy Office of Nuclear Energy (DOE NE). The response of AM materials to irradiation in reactor service environments is crucial for the reliability and safety of nuclear reactor components. Every new material to be used in reactor environments must be assessed for its irradiation response, and AM materials are not an exemption. Some microstructures unique to AM materials, such as compositional inhomogeneity and dislocation cell structure, are of particular importance since they may lead to different performance behavior under irradiation.

To understand the irradiation responses of AM materials, ion irradiations can be a critical tool. Compared with neutron irradiations, ion irradiations are more accessible, produce no or very low radioactivity, and have better controlled irradiation environments. More importantly, ion irradiations allow much more rapid displacement damage being generated in materials than neutron irradiations can do, decreasing the time needed for achieving high damage levels. Specimens can be irradiated to a few displacements per atom (dpa) in hours with ions rather than in years with neutrons. This enables a much shorter irradiation-characterization cycle, allowing a quick screening or exploration of different AM printing and post-processing conditions against irradiation damage. Nonetheless, the high damage rate with ions can also have a profound impact on damage production and evolution, leading to different microstructures between the ion and neutron irradiated specimens. To understand these differences, modeling and simulation are critical to understand the ion irradiation results in the context of simulating neutron damage in reactor service conditions. Irradiation phenomena accelerated, altered, or even absent in ion irradiations need to be analyzed with models to utilize the ion irradiation results for predicting the material's service performance in reactors.

This work package is to perform *in-situ* and *ex-situ* ion irradiations, as well as microstructural characterizations to support the development of AM materials for reactor applications. The objective is two-fold: (1) to quickly explore the irradiation responses of different AM materials in order to identify the influential factors contributing to the performance of AM materials under irradiations, and (2) to provide high-fidelity data in support of the development of irradiation damage models for AM materials, correlating ion and neutron irradiations. The ultima goal of this work is to support the AMMT's objective of using combined neutron and ion irradiation data to accelerate the qualification of AM materials for nuclear applications. This report

documented the experimental results of the *in-situ* and *ex-situ* ion irradiations and microstructural characterizations on LPBF316L and LPBF316H stainless steels (SS).

2 Experimental

The experimental effort focused on LPBF 316L and 316H SSs printed with laser power bed fusion (LPBF) process. AM 316L SS has been one of the most popular materials being produced with LPBF and some preliminary irradiation data are available in literature [1–4]. In the meantime, AM 316H SS is relatively new and no prior study on its irradiation performance exists to our knowledge. The experimental data collected in this study can be compared with wrought 316 SSs in literatures for understanding the difference between AM and wrought 316 SSs. This section discusses the experimental method, including the material fabrication, preparation of *in-situ* and *ex-situ* irradiation specimens, irradiation experiments, microstructural examinations and nanoindentation tests.

2.1 Materials and specimen preparations

Three AM builds were investigated in this study: LPBF316L-1, LPBF316L-2, and LPBF316H. Their compositions are given in Table 1. These AM prints were produced with LPBF at two laboratories. The LPBF316L-1 was printed at ORNL in the form of plates using a Concept Laser M2 system by GE. The same build has also been irradiated with neutrons and tested at ORNL [2]. The LPBF316L-2 and LPBF316H prints were produced at ANL in the form of small rectangular blocks using a Renishaw AM400 system. The printing parameters of these materials can be found in previous reports [5]. The composition of LPBF316L-1 shown in Table 1 was the nominal composition of powder provided by the vendor. The compositions of LPBF316L-2 and LPBF316H were measured by cutting a small piece from the build and analyzed with the combustion infrared detection for carbon, inert gas fusion for hydrogen, oxygen and nitrogen, and direct current plasma emission spectroscopy for other elements.

Table 1. Compositions (wt.%) of the LPBF316L and LPBF316H stainless steels

Materials	LPBF 316L	LPBF 316L	LPBF 316H
Build ID	20190308	20210421	20220217M
Oxygen	0.05	0.037	0.046
Nitrogen	0.01	0.095	0.015
Carbon	0.006	0.017	0.04
Sulfur	-	0.009	0.005
Iron	Bal.	Bal.	Bal.
Chromium	17.1	16.55	17.04
Manganese	1.19	0.57	1.09
Silicon	0.46	0.59	0.45
Nickel	12.1	12.33	12.22

Copper	0.01	0.12	0.007
Molybdenum	2.41	2.26	2.57
Vanadium	-	0.057	0.01
Phosphorus	<0.005	0.013	0.018
Cobalt	0.1	0.058	0.028
Tungsten	-	<0.002	<0.002

The printed materials were machined into 3-mm-diameter rods with an electrical discharge machine (EDM) along their build directions. Then, the rods were cut into 550 µm-thick disks with EDM. For *in-situ* ion irradiations, the disks were mechanically polished on both sides with sandpapers to a thickness around 100 µm, and then electropolished between -30ºC and -40ºC until perforation. The electrolyte used was composed of 5% perchloric acid and 95% methanol. For ex-situ ion irradiations, only one sides of the disks were polished. The polishing was performed with sandpapers down to P4000 grit, polycrystalline diamond suspension down to 1 µm, vibratory polishing using 50 nm colloidal silica polishing suspension, and finally electropolishing at -30ºC to -40ºC using the same electrolyte for 20-30 seconds.

2.2 *In-situ* and ex-situ ion irradiations

In-situ ion irradiations were performed in the IVEM-Tandem Facility at Argonne using a NEC implanter and a Hitachi-9000 TEM [6] (Figure 1). A Gatan double-tilt heating holder was used. The irradiation parameters are given in Table 2. For each in-situ irradiation experiment, bright-field (BF) mages, dark-field (DF) images and diffraction patterns were taken at 0.3 dpa, 0.6 dpa, 1 dpa, 3 dpa and 5 dpa to show the defect evolution as a function of dose. The vacuum of the TEM chamber was maintained below $3x10^{-7}$ torr throughout the in-situ irradiation experiments.

Ex-situ ion irradiations were performed with a tandem accelerator (Figure 2). The irradiation parameters are given in Table 3. The specimens were heated with a light bulb, and a thermocouple was attached to the specimen holder for temperature control. The vacuum of specimen chamber was maintained on the order of 10^{-7} torr during irradiation.

Figure 1. The IVEM-Tandem Facility at Argonne National Laboratory

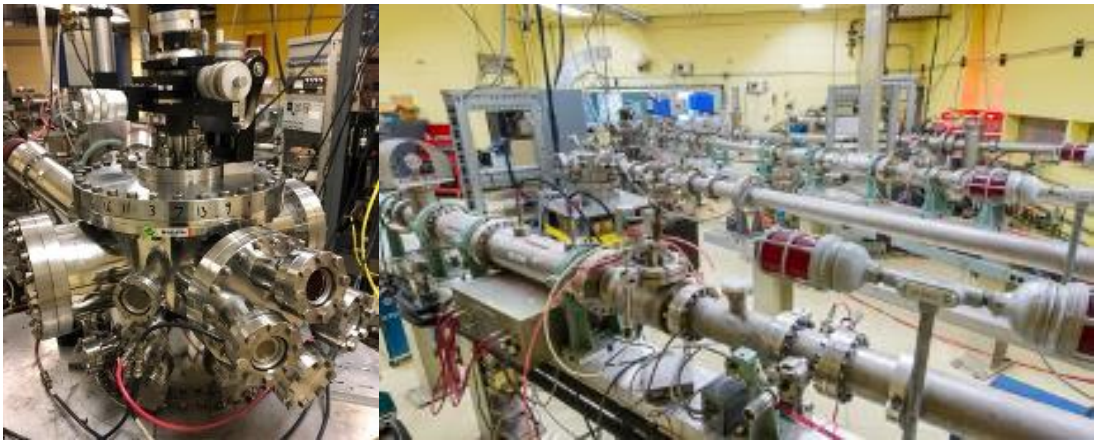

Figure 2. Specimen chamber and the beam lines for ex-situ ion irradiation.

Table 2. Irradiation parameters of *in-situ* ion irradiation

Materials	Ion	Temp (ºC)	Dose rate (dpa/s)	End Dose (dpa)
LPBF316L -1	1 MeV Kr^{2+}	600	10^{-3}	5
		300		
LPBF316L -2		600		
		300		
LPBF316H		600		
		300		

Table 3. Irradiation parameters of ex-situ ion irradiation

	Ion	Temp (ºC)	Dose rate (dpa/s)	Dose (dpa)	Nanoindentation
LPBF316L-1	4 MeV Ni^{2+}	600	10^{-3}	0.2	✓
				2	✓
				5	✓
				10	✓
			10^{-4}	0.2	
				2	
			10^{-5}	0.2	
		300	10^{-3}	0.2	
				2	
				5	
				10	
			10^{-4}	0.2	
				2	
			10^{-5}	0.2	

2.3 Post-irradiation examination

The as-printed LPBF316L and a LPBF316H *in-situ* irradiated at 600ºC were examined with EDS mapping on a Thermal Fisher Talos TEM in the Center for Nanoscale Materials at Argonne National Laboratory, with a focus on the dislocation cell structures, grain boundaries, and precipitates. Nanoindentation using a Bruker TI Premier was performed on as-printed and *ex-situ* irradiated specimens. Load pattern was 5-2-5 (5 sec for ramp-up, 2 sec for hold, and 5 sec for ramp-down). For each specimen, 100 indents were performed under load control. Hardness for a contact depth ranging from ~100 nm to ~220 nm was accessed.

3 Results and Discussion

3.1 TEM examinations of as-printed microstructures

Figure 3 shows the TEM results obtained from the as-printed LPBF316L-1 SS. Figures 3(a) and 3(b) show the dislocation cell structure resulting from the printing process. The average size of the cells, as measured from the short axis of the elliptical-shaped cells, is 505 ± 38 nm. Figure 3(c) shows the diffraction pattern taken under a two-beam condition near 001 zone axis. Figure 3(d) and Figure 3(e) are the magnified under-focused BF images showing small particles decorating the dislocation cell walls. Their average size is 18.5 nm, but some of the largest particles can be close to 100 nm, as shown in the size distribution plot in Figure 3(f). These particles are reported as (Si, Mn) oxides previously in literatures [2,3]. Besides the silicon oxides, large inclusions with a size of 1-2 μm have been observed occasionally in the TEM foil as shown in Figure 3(g). The corresponding EDS spectrum in Figure 3(h) indicates that the inclusion contains Mn, Cr, Si, Al, and O. The tantalum signal is from the specimen holder.

Figure 4 shows the TEM analysis of as-printed LPBF316L-2. Figure 4(a) shows the dislocation cell structure where the average cell size is 509.4 ± 51 nm. Figures 4(b) and 4(c) show the BF and DF images of a dislocation cell. Figure 5 shows the TEM analysis of as-received LPBF316H. Figure 5(a) is the low-magnification BF image showing the dislocation cell structures in the as-printed AM 316H SS. The cell size was measured to be 531 ± 75 nm. Similarly, silicon oxides were observed in LPBF316L-2 and LPBF316H decorating the dislocation cell walls. Inclusions like those in LPBF316L-1, Figure 3(g), were also observed in LPBF316L-2 and LPBF316H.

The elemental maps of as-printed LPBF316H are shown in Figure 6. The dislocation cell wall is enriched in Cr, Mo and, marginally, Si. Fe is depleted at the cell wall. The nanoparticles decorating the dislocation cell wall were enriched in Si, Mn, and O. No carbides were observed. The elemental distribution observed in LPBF316H is consistent with that of LPBF316L reported previously [3,7]. Overall, the as-printed LPBF316L-1, LPBF316L-2, and LPBF316H show similar microstructures, featuring dislocation cells in the order of 500 nm, small silicon oxide nanoparticles decorating the cell walls, and chemical inhomogeneity primarily along the cell walls.

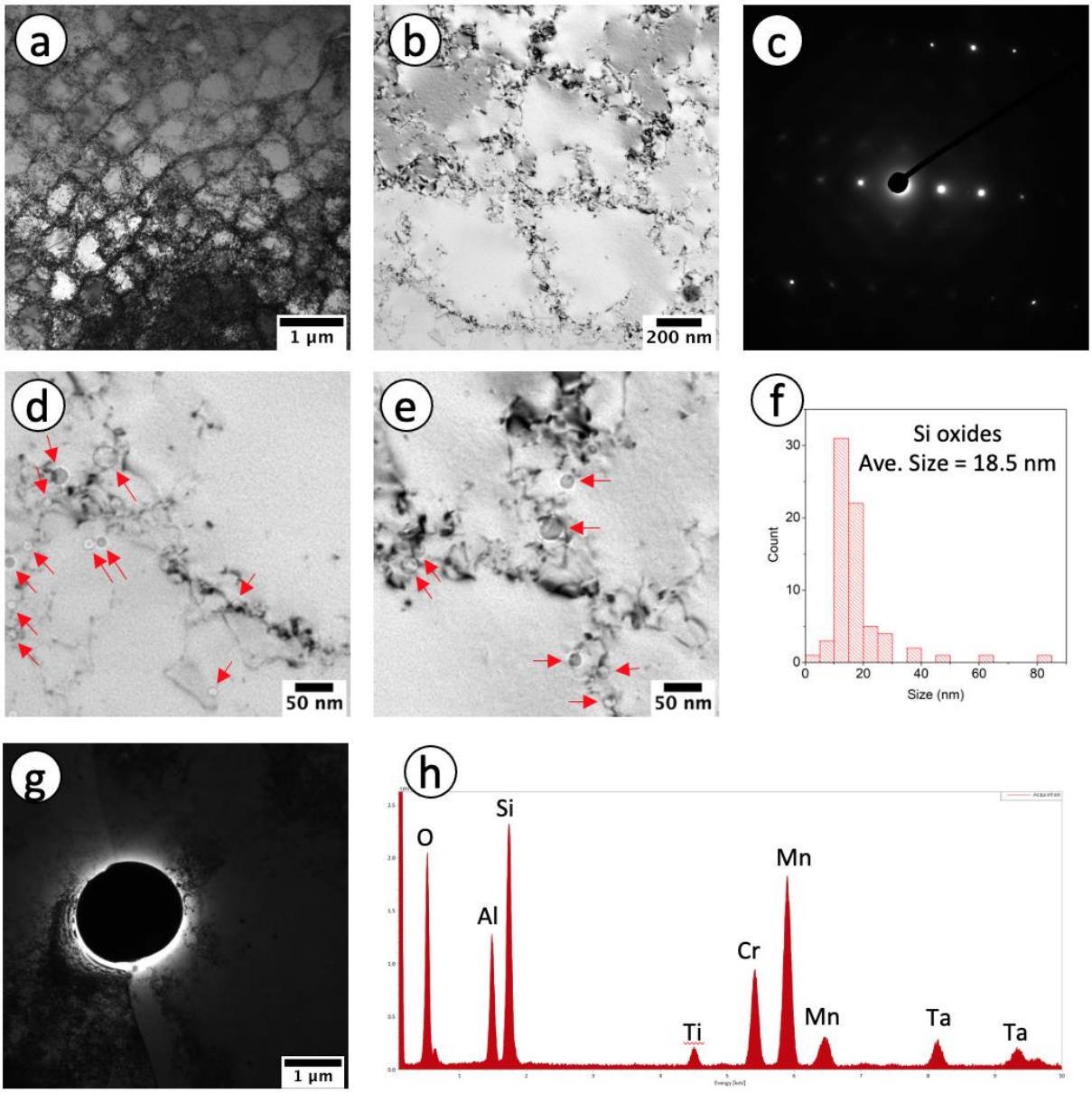

Figure 3. TEM results of as-printed LPBF316L-1: (a) low-magnification BF TEM image. (b) high-magnification BF TEM image. (c) diffraction pattern taken at a two-beam condition of g = 200 near 001 zone axis. (d)(e) under-focused TEM images with a defocus of 5 μm. The red arrows indicate the oxide particles. (f) the size distribution of the oxide particles. (g) TEM image of an inclusion. (h) EDS spectrum of the inclusion.

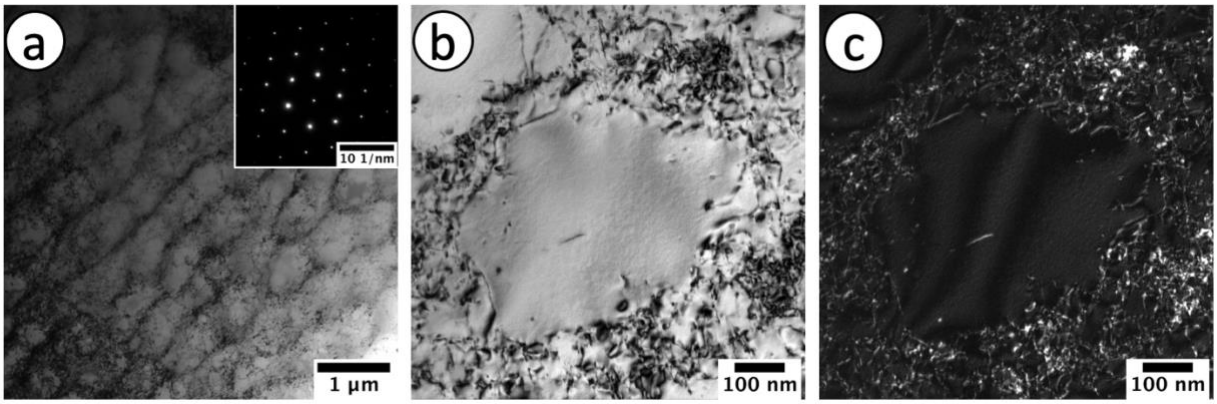

Figure 4. TEM images of as-printed LPBF316L-2: (a) low-magnification BF TEM image. The inset is the diffraction pattern taken at 011 zone axis. (b) BF TEM image of a dislocation cell. (c) the corresponding DF TEM image of the dislocation cell. The imaging condition for (b) and (c) is a two-beam condition with g = 200 near 011 zone axis.

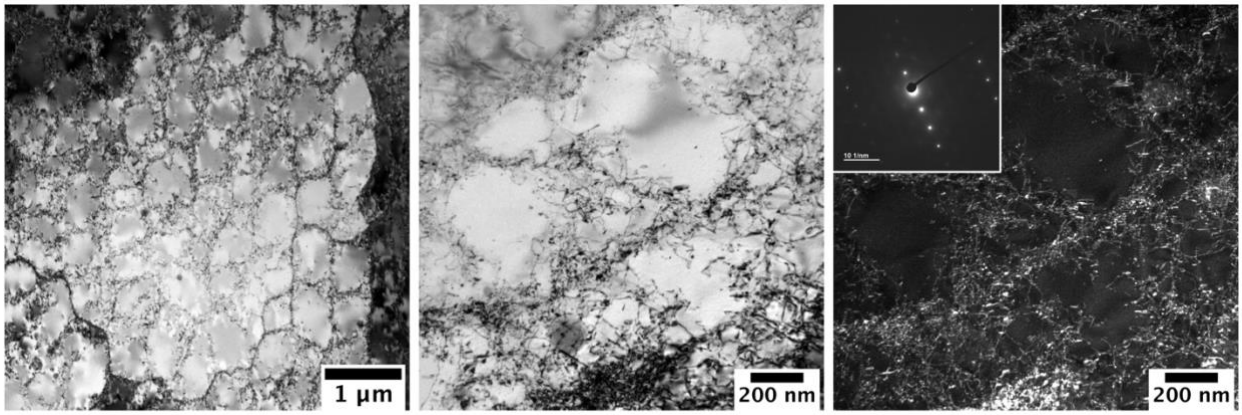

Figure 5. TEM images of as-printed LPBF316H SS: (a) Low-magnification BF TEM image. (b) and (c) Higher-magnification BF and DF TEM images of a dislocation cell. The inset is the corresponding diffraction condition for the images (g = 200 near 011 zone axis).

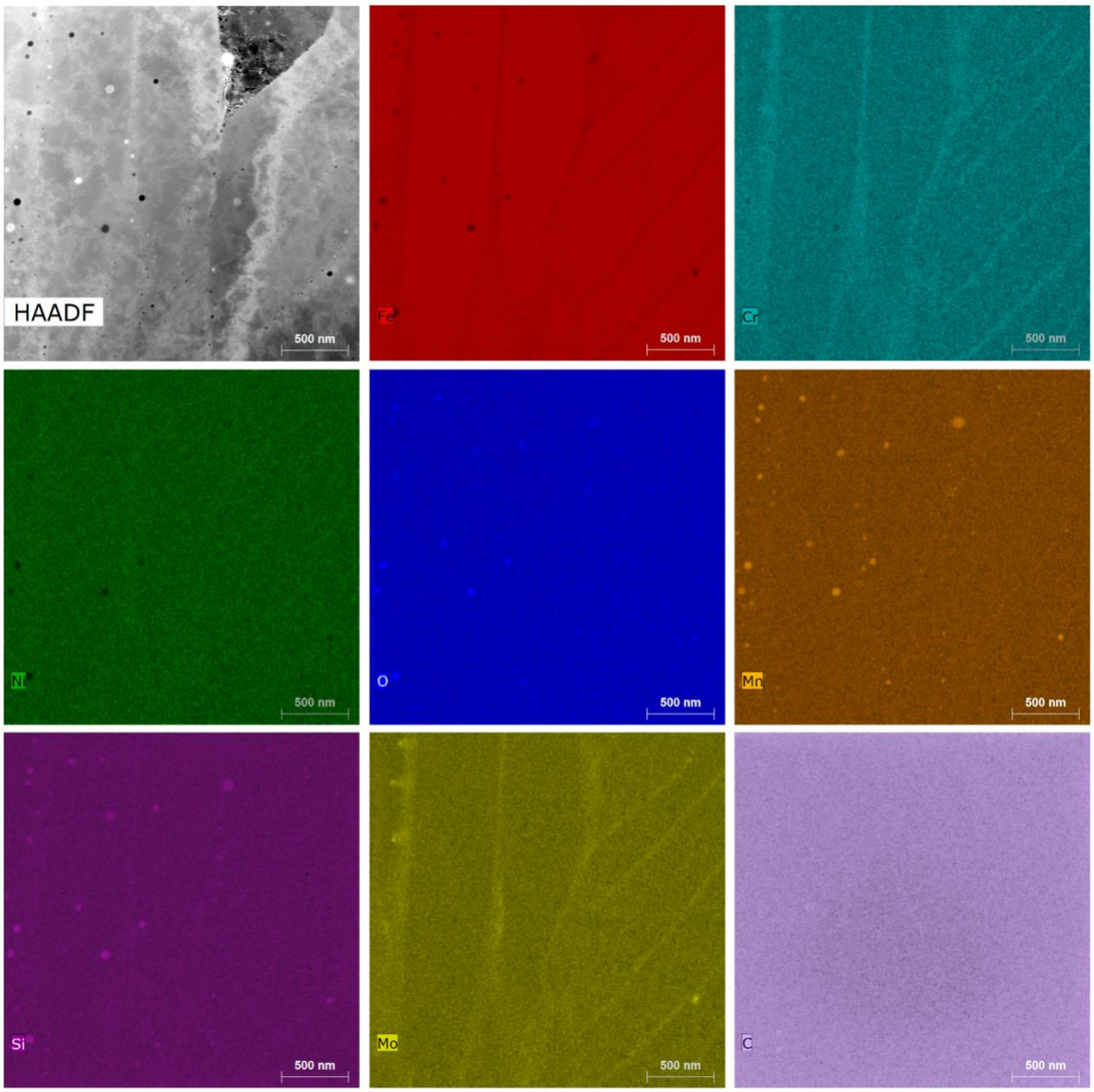

Figure 6. EDS composition maps of as-printed LPBF316H. Magnification is 20K.

3.2 Defect evolution under *in-situ* ion irradiation

3.2.1 Defect evolution in LPBF 316H SS

The microstructure of LPBF 316H SS continuously evolved under in-situ ion irradiations. Figure 7 and Figure 8 are two sets of TEM images taken from the same areas during the 600°C and 300°C in-situ irradiations, respectively. For the irradiation at 600ºC, the irradiation-induced dislocation loops formed first near the center of the dislocation cells, which was defect free prior to the irradiation. The preexisting cell walls tend to become thinner under irradiation, but no dislocation loops can be resolved inside the cell walls. The different responses to irradiation between the cell interior and cell walls indicate an effect of the dislocation cell structure on the loop formation. Both 1/3<111> faulted loops and ½<110> perfect loops were

observed at 600°C, and there was no obvious difference between the two types of dislocation loops in their location relative to the cell structure. With increasing irradiation dose, the loop size increased, and more loops were formed filling up the empty space inside the as-printed cell structure. At 3 dpa (Figure 7d), irradiation-induced dislocation loops had occupied the entire cell interior. As the loop density and size increased, the frequency of the loop-loop interaction increased and eventually led to the formation of dislocation network as observed at 5 dpa (Figure 7e). The as-printed heterogeneous dislocation cell structure was replaced by a uniform dislocation network beyond 5 dpa, and the prior cell walls were barely visible at high doses. It should be noted that, however, the observed defect evolution as a function of dose can be affected by foil-thickness. At a different foil thickness, while the general trend of defect evolution would remain the same, the exact doses for the different stages of the evolution may be different.

In contrast to the results of 600ºC irradiation, the formation of irradiation-induced dislocation loops was less affected by the dislocation cell structure in the 300ºC irradiation. As shown in Figure 8(a), even at the lowest dose of 0.3 dpa, a high density of dislocation loops was observed uniformly distributed within the preexisting dislocation cells. The dislocation walls became less organized under irradiation and quickly vanished with the increasing dose. Up to 1 dpa, the majority of the irradiation-induced dislocation loops were small, and difficult to characterize their Burgers vectors. However, as shown in Figure 8(f), some of the irradiation-induced dislocation loops can be determined as 1/3<111> faulted loops based on their edge-on appearance under the corresponding crystallographic orientation. With the increasing irradiation dose, extended defects, such as large dislocation loops and dislocation segments, were observed at 3 and 5 dpa, and the density of dislocation loops decreased, which indicates the coalescence between irradiation-induced dislocation loops at high doses. No voids were observed at either irradiation temperatures.

3.2.2 Defect evolution in LPBF 316L SS

Similar to that of LPBF 316H SS, the microstructure of LPBF 316L SS evolved as well with increasing dose under in-situ ion irradiations performed at 600°C and 300°C. The observations made in these in-situ experiments were consistent with a previous study on a different LPBF316L build reported in reference [3]. Figure 9 and Figure 10 show the TEM images of LPBF316L-1 and LPBF316L-2, respectively, irradiated at 600ºC to 1 dpa. Like the LPBF316H, large 1/3<111> faulted loops and ½<110> perfect loops were produced by irradiation preferentially at the interior of dislocation cells. Figure 11 and Figure 12 show the TEM images of LPBF316L-1 and LPBF316L-2, respectively, irradiated at 300ºC to 1 dpa. Again, a high density of small dislocation loops was observed uniformly within the cell structure. The loop size and density were different among the three materials, LPBF316L-1, LPBF316L-2, and LPBF316H, making it possible to study the compositional effect (e.g. 316L vs 316H) on irradiation damage. However, since TEM foil surfaces are defect sinks that could strongly affect the defect evolution [8,9], a careful analysis of foil thickness is essential to make quantitative comparisons among different samples.

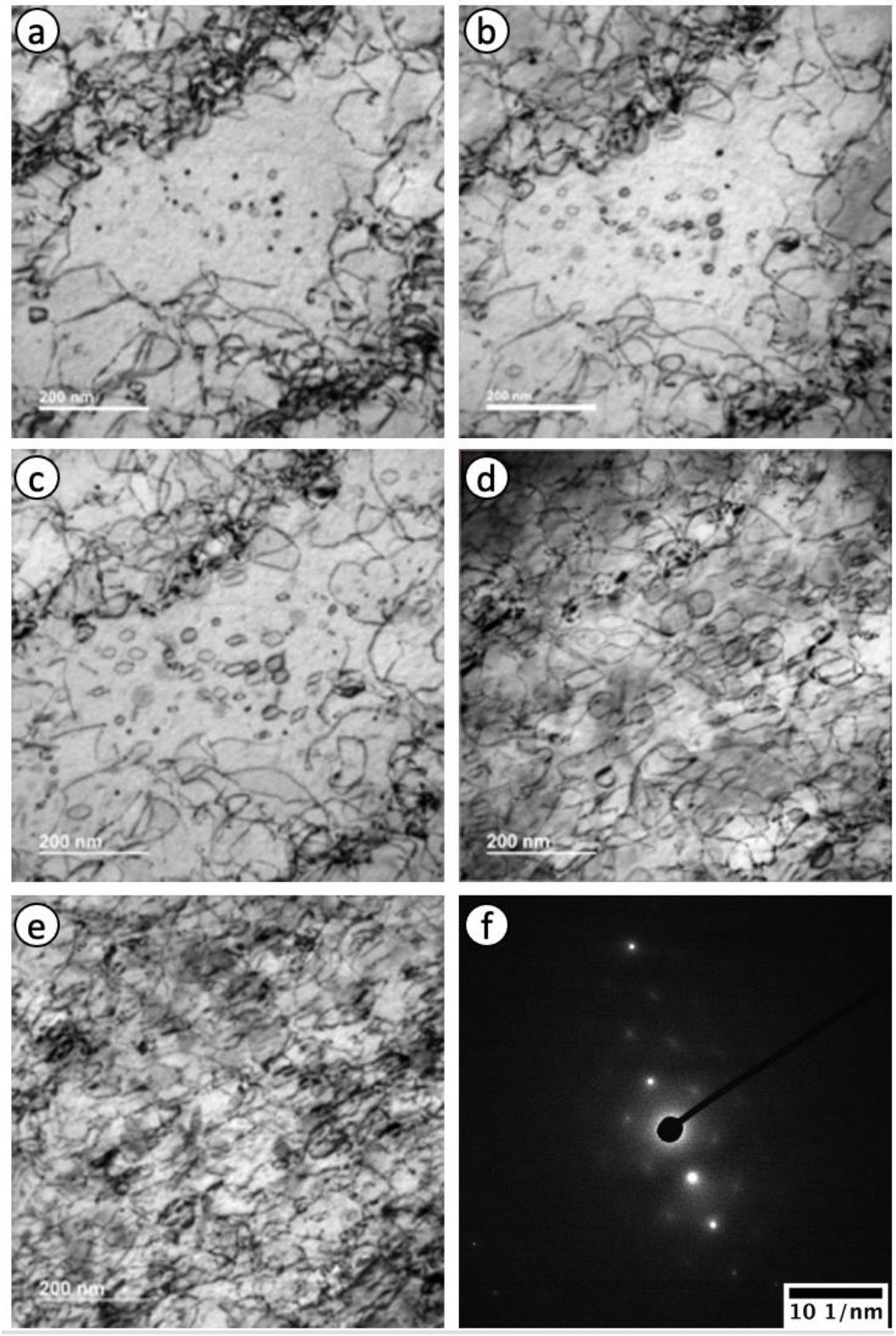

Figure 7. A set of same area BF TEM images of LPBF316H *in-situ* irradiated with 1 MeV Kr ions at 600ºC to (a) 0.3 dpa, (b) 0.6 dpa, (c) 1 dpa, (d) 3 dpa and (e) 5 dpa. (e) the corresponding diffraction pattern of the two-beam condition (g = 200 near 011 zone axis) used for the set.

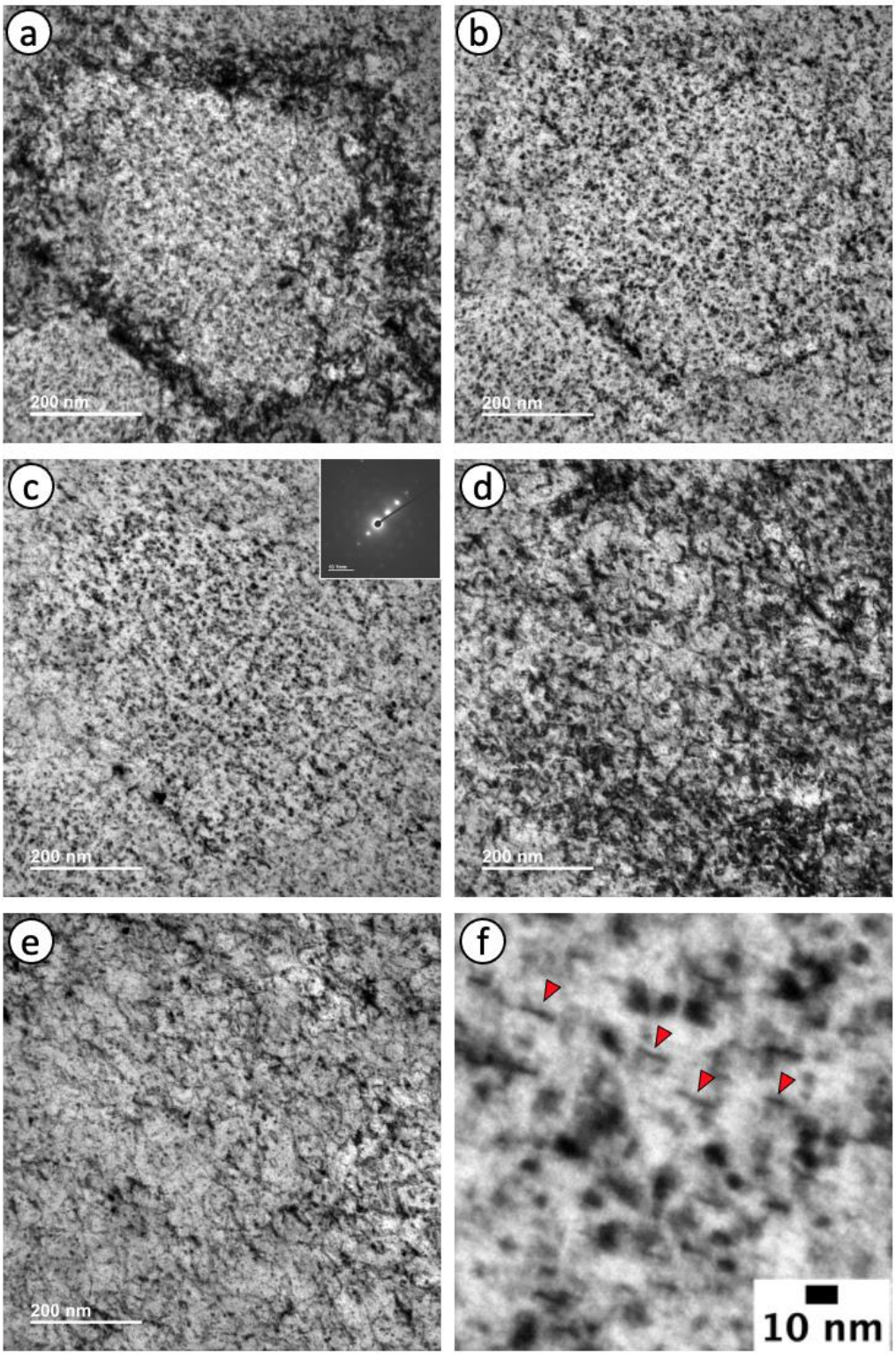

Figure 8. A set of same area BF TEM images of LPBF316H *in-situ* irradiated with 1 MeV Kr ions at 300ºC to (a) 0.3 dpa, (b) 0.6 dpa, (c) 1 dpa, (d) 3 dpa and (e) 5 dpa. The inset is the diffraction pattern indicating the two-beam condition of g = 200 near 011 zone axis. (f) a high-magnification image of the 1-dpa sample. The red arrows indicate the edge-on faulted dislocation loops.

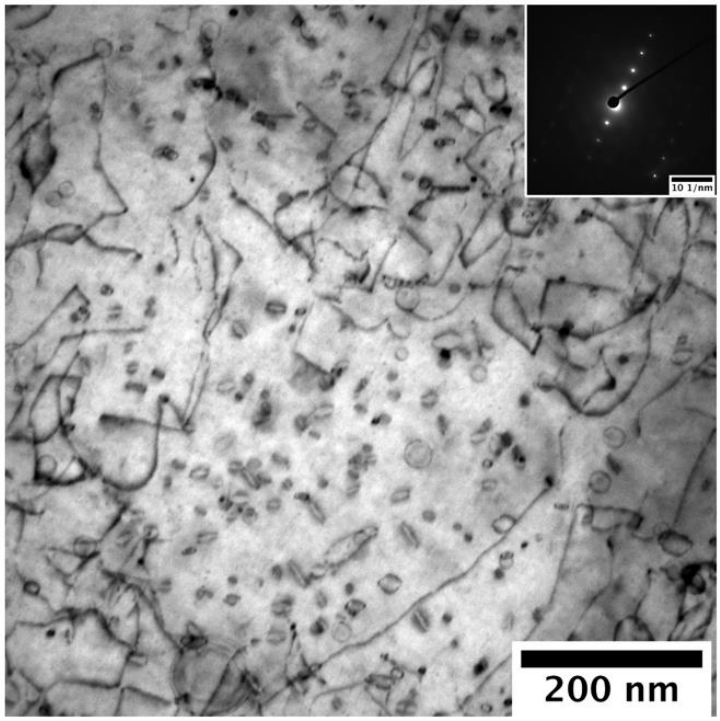

Figure 9. BF TEM image of LPBF316L-1 *in-situ* irradiated with 1 MeV Kr ions at 600ºC to 1 dpa. The inset is the imaging condition -- a two-beam condition with g = $\mathbf{11\bar{1}}$ near 011 zone axis.

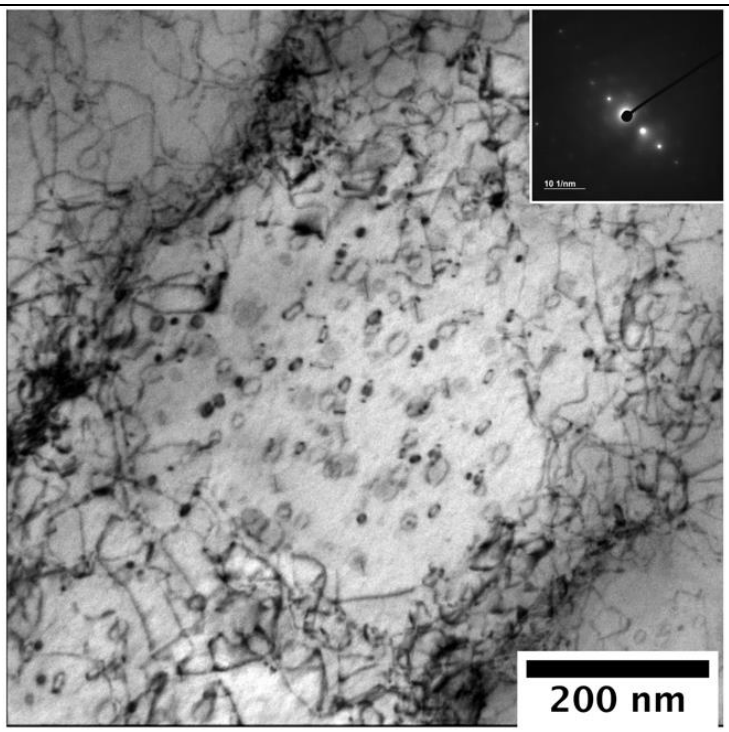

Figure 10. BF TEM image of LPBF316L-2 *in-situ* irradiated with 1 MeV Kr ions at 600ºC to 1 dpa. The inset diffraction pattern is the imaging condition -- a two-beam condition with g = 200 near 011 zone axis.

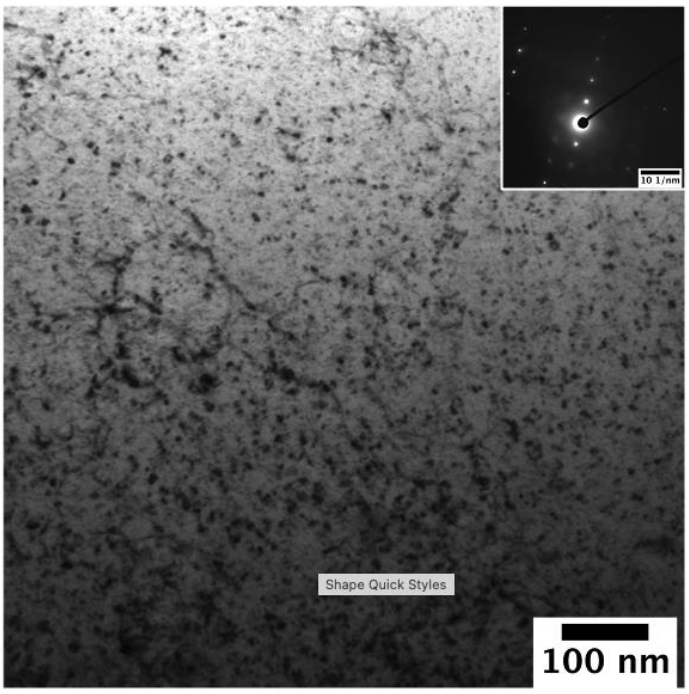

Figure 11. BF TEM image of LPBF316L-1 *in-situ* irradiated with 1 MeV Kr ions at 300ºC to 1 dpa. The inset diffraction pattern is the imaging condition -- a two-beam condition with g = 200 near 001 zone axis.

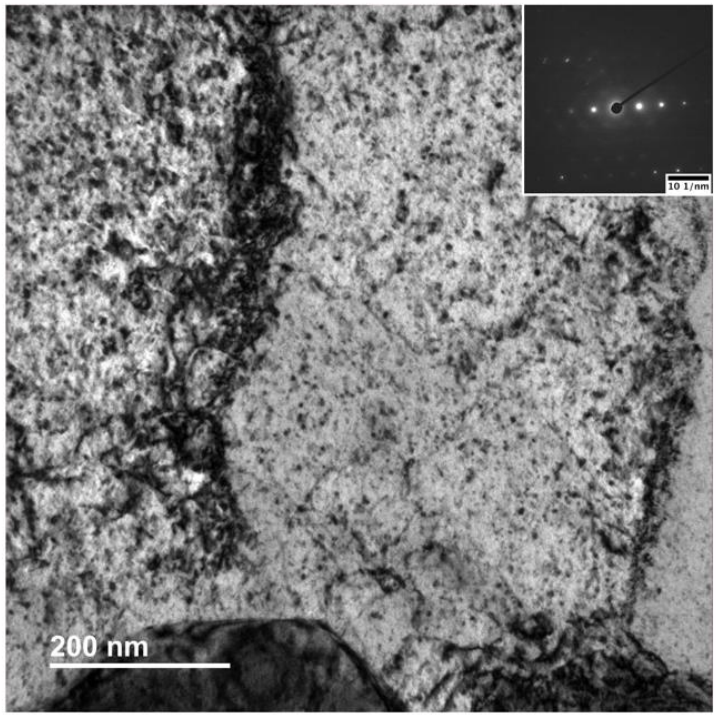

Figure 12. BF TEM image of LPBF316L-2 *in-situ* irradiated with 1 MeV Kr ions at 300ºC to 1 dpa. The inset diffraction pattern shows the imaging condition -- a two-beam condition with g = 200 near 011 zone axis.

3.2.3 RIS in LPBF316H SS

Figure 13 shows the elemental maps of LPBF316H irradiated at 600ºC to 5 dpa. Irradiation-induced segregation (RIS) at grain boundaries was observed. Cr and Mn were depleted, while Si, Ni and some trace amounts of O were enriched. No carbides were observed after the irradiation. Instead, a high density of small Cr-rich oxide rods with a length of 50-100 nm and a width of 10-20 nm were observed. The presence of such a high density of nanoparticles can have an impact on mechanical properties and therefore is worth further investigation. Figure 14 shows the elemental maps of an LPBF316H TEM specimen annealed at 600ºC inside the TEM for 90 minutes. The temperature and duration of the annealing are identical to the in-situ irradiation performed at 600ºC to 5 dpa. Without irradiation, no Cr-rich oxides were formed in the annealed sample, which indicates that the formation of Cr-rich oxide in the irradiated LPBF316H was an irradiation effect. Oxygen enrichment at grain boundaries, however, were similar between the annealed and irradiated specimens. On the other hand, a previous study on an LPBF316L sample solution annealed at 1050ºC for 30 minutes also showed the formation of Cr-rich oxides [10]. Further investigation on the effects of irradiation and the thermal stability of the Cr-rich oxides is required.

Besides, the Cr and O maps in Figure 13 show a denuded zone, with a width of ~200 nm, in the vicinity of grain boundary. The denuded zone free of oxide particles, however, is less evident along the grain boundary of another area shown Fig. 15. In addition, the density of oxide particles seems nonuniform among different grains. In Fig. 13, the amount of Cr oxides appears

to be more in the upper-left grain than in the lower-right grain. Similar observations can also be made for Figure 15.

Regarding the existing chemical inhomogeneity resulting from printing process, the depletion of Fe and the enrichment of Ni and Mo at cell walls largely survived after irradiations. The enrichment of Cr at cell walls after irradiation, however, requires further investigation. Finally, the preexisting (Si, Mn) oxide nanoparticles inside the AM specimens remained stable after irradiation.

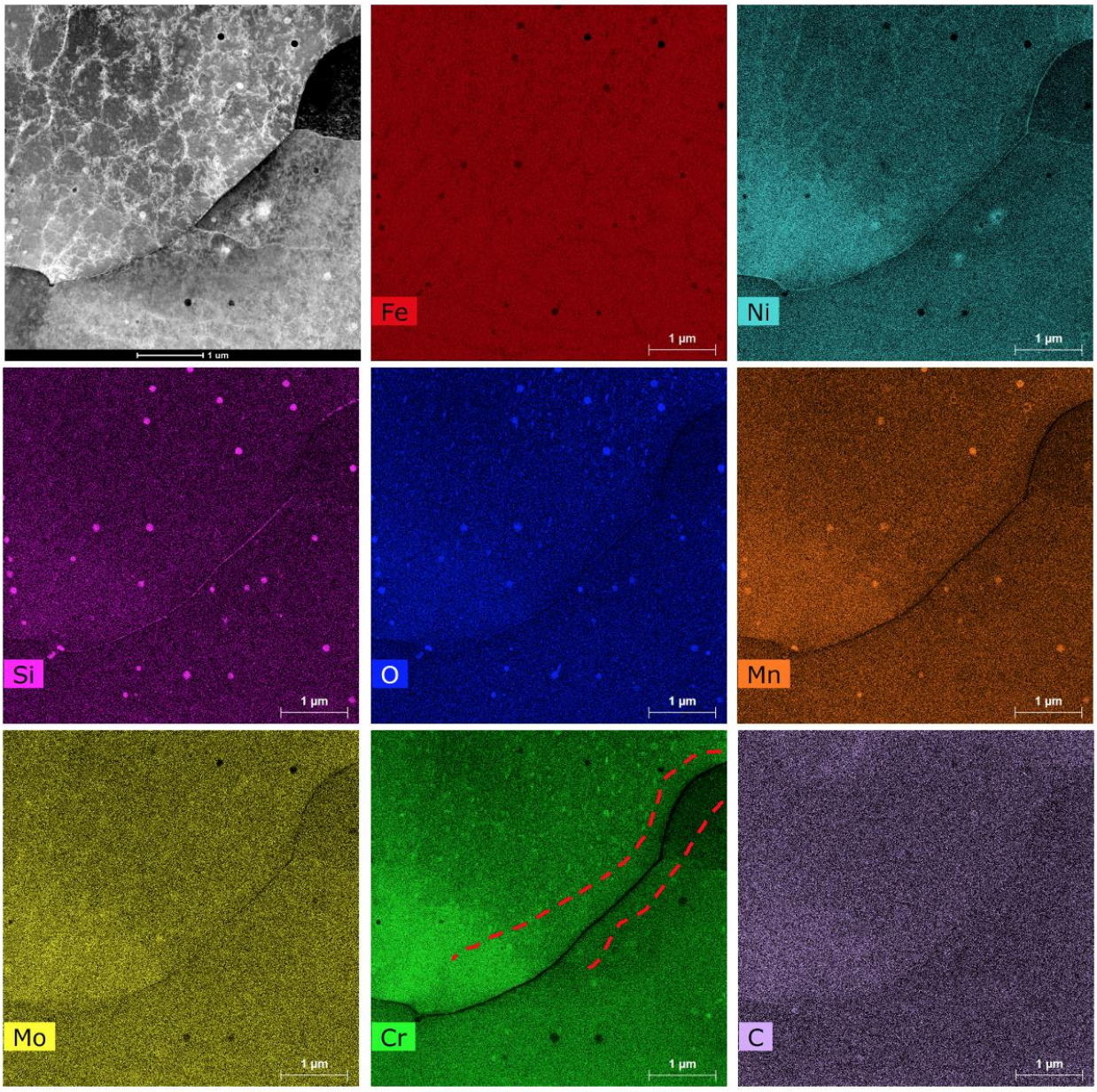

Figure 13. EDS maps of LPBF316H *in-situ* irradiated at 600ºC with 1 MeV Kr ions to 5 dpa. The red dashed curves highlight the boundary of a denuded zone of chromium oxides in the vicinity of the grain boundary. All the EDS maps were characteristic x-ray intensity maps, except for iron, which is a compositional map. The magnification is 20K.

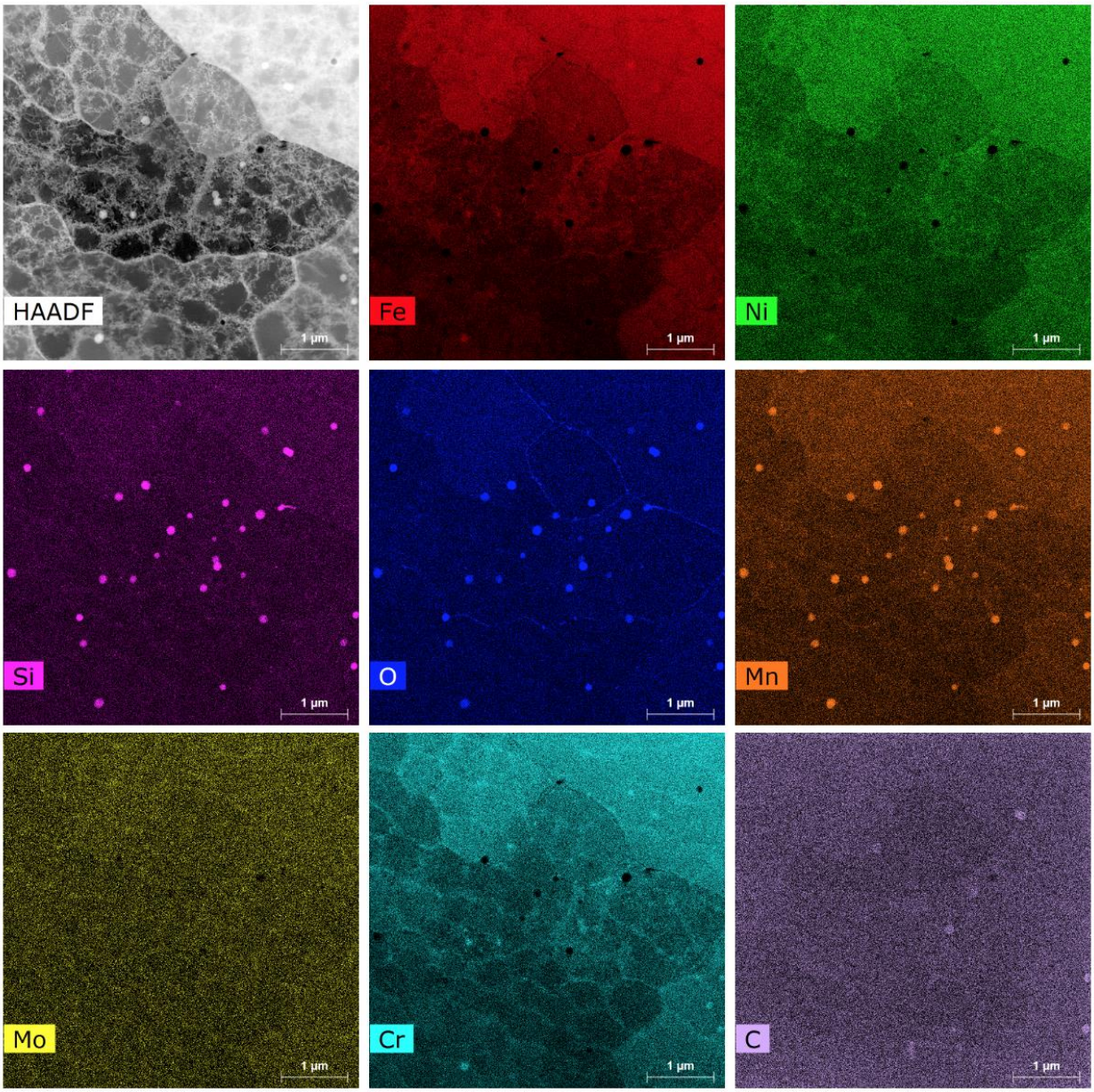

Figure 14. EDS maps of LPBF316H annealed at 600ºC inside a TEM for 90 minutes. All maps are intensity maps. The magnification is 20K.

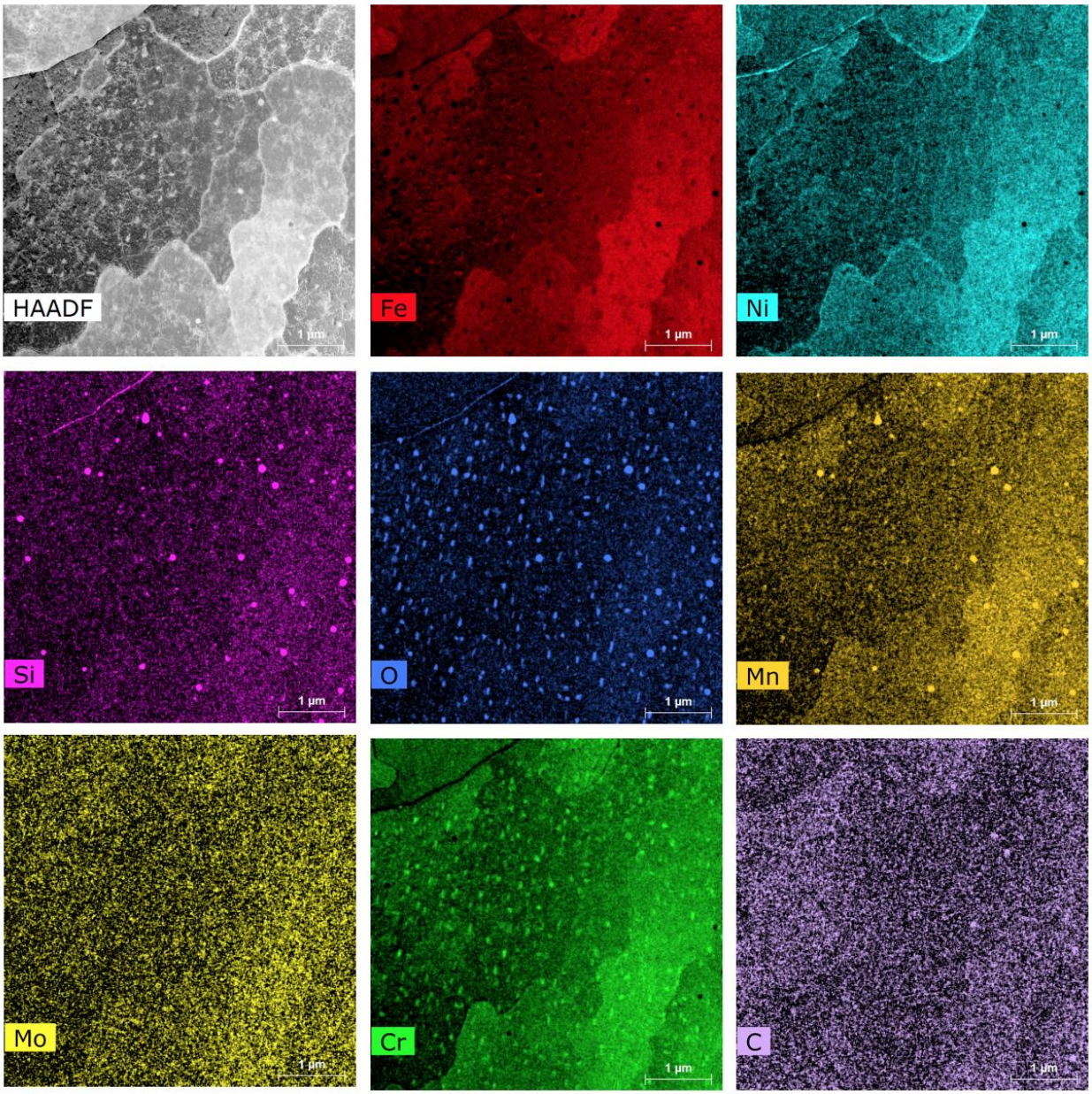

Figure 15. EDS maps of LPBF316H *in-situ* irradiated at 600ºC with 1 MeV Kr ions to 5 dpa. All elemental maps are the characteristic x-ray intensity maps. The magnification is 20K.

3.3 Nanoindentation tests on ex-situ irradiated specimens

The *ex-situ* ion irradiations on LPBF316L-1 shown in Table 3 have been completed. Nanoindentation tests were performed on the as-printed and 600°C-irradiated specimens.. The tests were carried out in a load-controlled mode with a maximum load of 4000 µN and a loading rate of 800 µN/s. Figure 16 shows the hardness as a function of contact depth. A general trend of decreasing hardness with increasing contact depth can be seen for all samples regardless their irradiation conditions. For all specimens, a considerable scattering of hardness data was observed. Therefore, sufficient data points need to be collected to reveal any effect of irradiation

dose. In the figure, the results from different doses are color coded. Each dot corresponds to one indentation measurement. The lines are the linear regressions of the data at the given doses, and the shaded areas indicate the 95% confidence level around the regression line. At 0.2 dpa, irradiation did not seem to change the hardness, and the data points from the as-printed and 0.2-dpa samples are practically indistinguishable. At 2 dpa, the hardness decreased slightly from the unirradiated state, indicating an irradiation softening behavior. At 5 and 10 dpa, the trend reversed, and the hardness increased with irradiation dose. As compared with the as-printed specimen, the extent of hardening was about 11-14% for the range of contact depth explored. This complex dose dependence of nanohardness results is consistent with the recent tensile tests on neutron-irradiated AM samples [2].

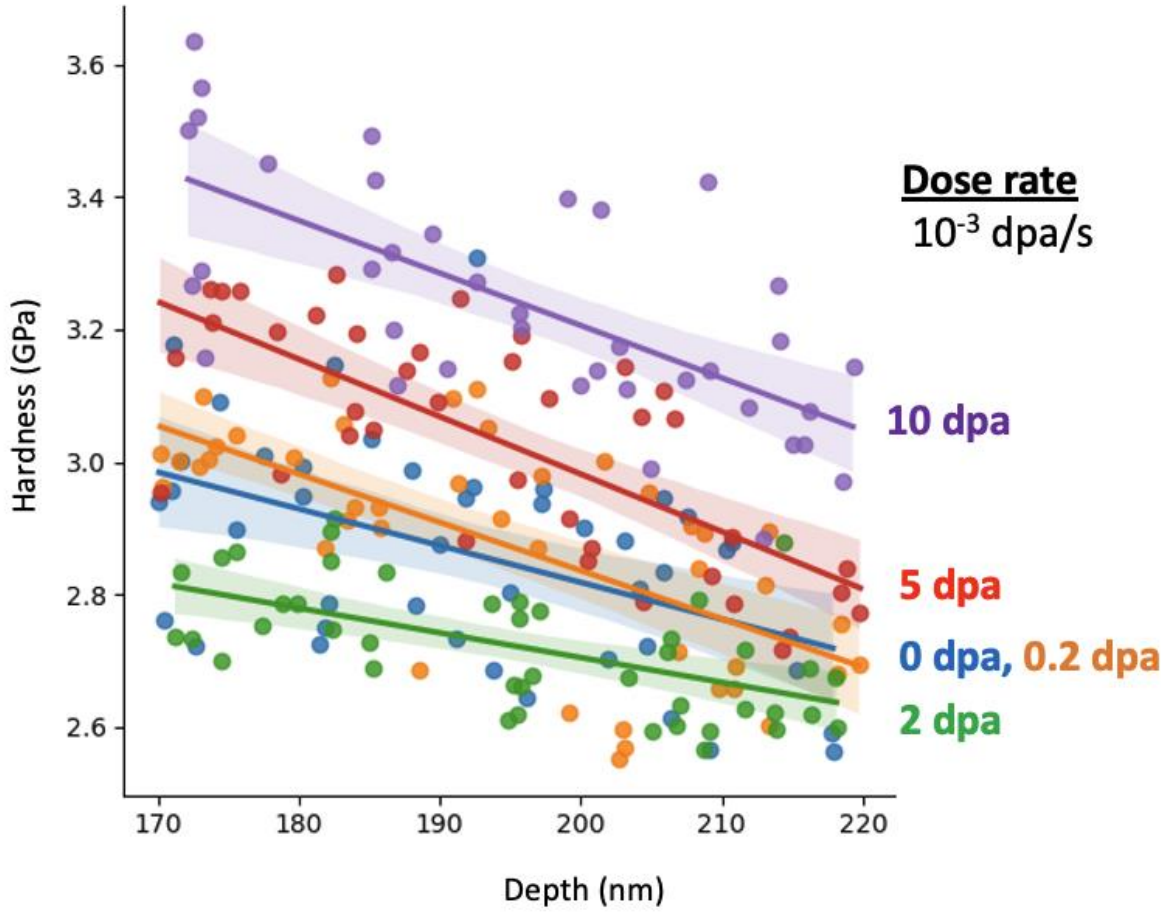

Figure 16. Load-controlled nanoindentation measurements on LPBF316L-1 irradiated with 4 MeV Ni ions at 600ºC.

4 Summary

The irradiation effects on LPBF316L and LPBF316H SS have been investigated through *in-situ* and ex-situ ion irradiations. As-printed LPBF316H and LPBF316L SS were found to share a similar dislocation cell structure with an average cell size of 505-531 nm. LPBF 316H and LPBF 316L behaved similarly under the *in-situ* irradiation with 1 MeV Kr ions. For the irradiation at 600ºC, a few faulted and perfect dislocation loops were formed initially at the centers of dislocation cells. With increasing dose, the loops grew and gradually populated the entire dislocation cells. At high doses, the initial dislocation cell structure was replaced by dislocation network. For the irradiation at 300ºC, a high density of small dislocation loops was formed quickly at low doses and uniformly distributed within the preexisting dislocation cells. The dislocation cell structure does not significantly affect the spatial distribution of dislocation loops at this temperature. At high doses, extended dislocation structures were formed due to the coalescence of dislocation loops.

The effect of RIS was observed in LPBF316H irradiated at 600ºC. While Si, Ni and O were enriched at grain boundaries, Mn and Cr were depleted. For the existing compositional inhomogeneity at cell boundaries, the Ni and Mo enrichments and Fe depletion were still visible after irradiation, but the extents may have reduced. In addition, the existing Cr enrichment at cell walls was replaced with dense Cr-rich oxide nanoparticles. These Cr-rich oxides were not observed in the sample exposed to the same temperature without irradiation.

Ex-situ ion irradiation has been performed on LPBF316L SS at 600ºC and 300°C with 4 MeV Ni ions at three dose rates, 10^{-3} dpa/s (up to 10 dpa), 10^{-4} dpa/s (up to 2 dpa), and 10^{-5} dpa/s (up to 0.2 dpa). The results of nanoindentation tests performed on the 600ºC samples showed a complex dose dependence. The sample was softened at low doses but became harder as the dose continued to increase.

Acknowledgment

This work was sponsored by the U.S. Department of Energy, Office of Nuclear Energy, Advanced Materials and Manufacturing Technologies (AMMT) program, under Contract No. DE-AC02-06CH11357 with Argonne National Laboratory, managed and operated by UChicago Argonne LLC. . Dr. Xuan Zhang from Argonne National Laboratory and Dr. Thak Sang Byun from Oak Ridge National Laboratory are thanked for providing the materials used for this study.

References:

[1] M. Song, M. Wang, X. Lou, R.B. Rebak, G.S. Was, Radiation damage and irradiation-assisted stress corrosion cracking of additively manufactured 316L stainless steels, J. Nucl. Mater. 513 (2019) 33–44.

[2] T.S. Byun, B.E. Garrison, M.R. McAlister, X. Chen, M.N. Gussev, T.G. Lach, A. Le Coq, K. Linton, C.B. Joslin, J.K. Carver, F.A. List, R.R. Dehoff, K.A. Terrani, Mechanical behavior of additively manufactured and wrought 316L stainless steels before and after neutron irradiation, J. Nucl. Mater. 548 (2021) 152849. https://doi.org/https://doi.org/10.1016/j.jnucmat.2021.152849.

[3] S. Li, J. Hu, W.Y. Chen, J. Yu, M. Li, Y. Wang, Evolution of cellular dislocation structures and defects in additively manufactured austenitic stainless steel under ion irradiation, Scr. Mater. 178 (2020) 245–250. https://doi.org/10.1016/J.SCRIPTAMAT.2019.11.036.

[4] Z. Shang, C. Fan, J. Ding, S. Xue, A. Gabriel, L. Shao, T. Voisin, Y.M. Wang, T. Niu, J. Li, T.D. de la Rubia, H. Wang, X. Zhang, Heavy ion irradiation response of an additively manufactured 316LN stainless steel, J. Nucl. Mater. 546 (2021) 152745. https://doi.org/https://doi.org/10.1016/j.jnucmat.2020.152745.

[5] B. Alexandreanu, X. Zhang, Y. Chen, W.-Y. Chen, M. Li, Mechanical Testing of Additively Manufactured Materials, No. ANL/NSE-22/83, Argonne National Laboratory, Argonne, IL, 2022.

[6] M. Li, W.-Y. Chen, P.M. Baldo, In situ transmission electron microscopy with dual ion beam irradiation and implantation, Mater. Charact. 173 (2021). https://doi.org/10.1016/j.matchar.2021.110905.

[7] Y.M. Wang, T. Voisin, J.T. McKeown, J. Ye, N.P. Calta, Z. Li, Z. Zeng, Y. Zhang, W. Chen, T.T. Roehling, R.T. Ott, M.K. Santala, P.J. Depond, M.J. Matthews, A. V. Hamza, T. Zhu, Additively manufactured hierarchical stainless steels with high strength and ductility, Nat. Mater. 17 (2017) 63–71. https://doi.org/10.1038/nmat5021.

[8] M. Li, M.A. Kirk, P.M. Baldo, D. Xu, B.D. Wirth, Study of defect evolution by TEM with in situ ion irradiation and coordinated modeling, Philos. Mag. 92 (2012) 2048–2078. https://doi.org/10.1080/14786435.2012.662601.

[9] W.-Y. Chen, M. Li, TEM study of nickel under in-situ helium/krypton dual-beam irradiation, in: Trans. Am. Nucl. Soc., 2019.

[10] M. Li, X. Zhang, W.-Y. Chen, T.S. Byun, Creep behavior of 316 L stainless steel manufactured by laser powder bed fusion, J. Nucl. Mater. 548 (2021). https://doi.org/10.1016/j.jnucmat.2021.152847.

Nuclear Science and Engineering Division
Argonne National Laboratory
9700 South Cass Avenue, Bldg. 212
Argonne, IL 60439

www.anl.gov